INTERNATIONAL JOURNAL FOR NUMERICAL METHODS IN FLUIDS
Int. J. Numer. Meth. Fluids 2003; **43**:483–505 (DOI: 10.1002/fld.500)

Predictability and uncertainty in CFD

D. Lucor*,†, D. Xiu, C.-H. Su and G. E. Karniadakis‡

Division of Applied Mathematics, Brown University, Providence RI 02912, U.S.A.

SUMMARY

CFD has reached some degree of maturity today, but the new question is how to construct simulation error bars that reflect uncertainties of the physical problem, in addition to the usual numerical inaccuracies. We present a fast Polynomial Chaos algorithm to model the input uncertainty and its propagation in incompressible flow simulations. The stochastic input is represented spectrally by Wiener–Hermite functionals, and the governing equations are formulated by employing Galerkin projections. The resulted system is deterministic, and therefore existing solvers can be used in this new context of stochastic simulations. The algorithm is applied to a second-order oscillator and to a flow-structure interaction problems. Open issues and extensions to general random distributions are presented. Copyright © 2003 John Wiley & Sons, Ltd.

KEY WORDS: computational fluid dynamics; polynomial chaos; Wiener–Hermite functionals; incompressible flows

1. INTRODUCTION

Computational fluid dynamics (CFD) is a mature discipline today. After more than 40 years of intense research efforts, starting with the seminal work of Harlow and Fromm in simulating unsteady flow past a cylinder (1965) [1], finite differences and finite element/volume methods are employed routinely in three-dimensional unsteady flow simulations. High-order methods and methods for complex-geometry domains have been advanced considerably, and numerical accuracy is adequately quantified in many simulations. While fully adaptive simulations are limited to some demonstration examples at the moment, at least the algorithmic framework and mesh generation technology exist for routine *adaptive* CFD in the near future.

In turbulence simulations, in particular, there has been some dramatic progress, and direct numerical simulation (DNS) has been the prevailing tool for analysing accurately the physics of turbulence at *all* scales albeit at modest Reynolds numbers. This development, which coincides with the birth of supercomputing in the mid-1970s and has greatly benefited from

* Correspondence to: D. Lucor, Division of Applied Mathematics, Brown University, Providence, RI 02912, U.S.A.
† E-mail: didi@cfm.brown.edu
‡ E-mail: gk@cfm.brown.edu

Contract/grant sponsor: ONR
Contract/grant sponsor: DOE

Received 1 April 2002
Accepted 15 January 2003

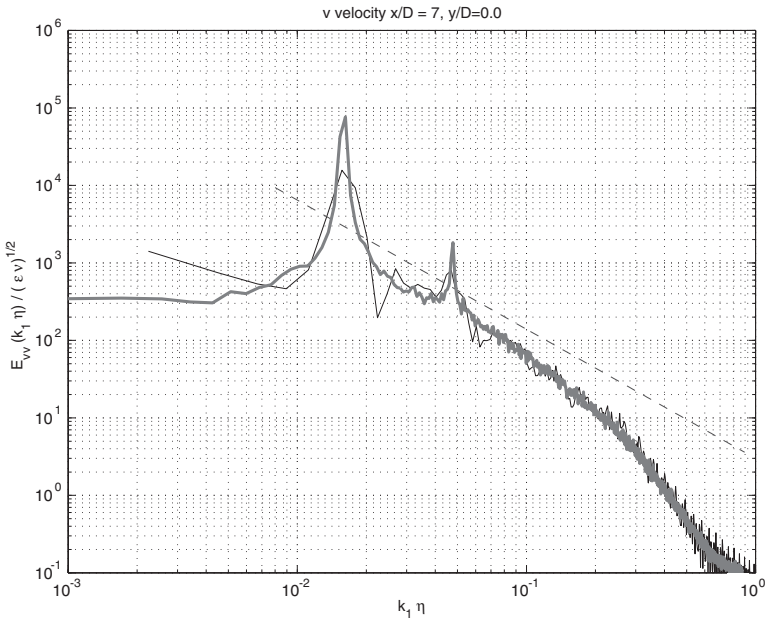

Figure 1. Cross-flow velocity spectrum at a centreline point seven diameters behind a cylinder. DNS (thin line) versus experiment of Ong and Wallace (thick line); $Re = 3900$, taken from [5].

it, has proved erroneous the pessimistic forecast that simulations of turbulence based on first principles could never be achieved [2, 3]. Fast solvers and teraflop speeds of today have allowed accurate DNS not only in canonical domains, such as turbulent channel flows [4], but also in spatially developing flows involving more complex-geometry domains.

An example of such DNS is shown in Figure 1, where we plot the results of the energy spectrum predicted by a spectral discretization involving about 100 million degrees of freedom [5]. In particular, the flow past a circular cylinder is simulated at $Re = 3900$ corresponding to a turbulent wake. In the figure we plot the one-dimensional wave number spectrum of the cross-flow velocity at a centreline location seven diameters behind the cylinder. Both axes are normalized with Kolmogorov scaling at $Re = 3900$, and a comparison of the DNS predictions with the experimental results of Ong and Wallace is included [6]. Very good agreement is obtained in the inertial range and in capturing the vortex shedding and shear layer frequencies, i.e. the two pronounced peaks in the plot of Figure 1. Surprisingly, the agreement is less satisfactory in the large scales (i.e. low wave numbers) which are clearly fully resolved.

The large scales are influenced by the domain size and by the specific form of the boundary conditions imposed on the truncated domain. More tests with larger domains are required, but at such high resolutions systematic tests cannot be easily performed. Moreover, even with the larger domain it is not clear that matching the outer flow with the experimental conditions can be achieved. There are many uncertainties associated with the experiment itself that have not been quantified; in fact, some uncertainties are *irreducible* and cannot be precisely quantified.

This example raises the issue of uncertainty in the boundary conditions and the experimental input but there are many more sources of uncertainty that can be present in simulating fluid

flows, laminar or turbulent, in a simple setting or in multi-disciplinary problems. In addition to boundary and initial conditions, there is still an uncertainty component associated with the physical problem, and specifically with such diverse factors as constitutive laws, transport coefficients, source and interaction terms, geometric irregularities (e.g. roughness), etc. With the CFD field reaching now some degree of maturity and with petaflop resources within the horizon, it is timely to pose the more general question of how to model uncertainty and stochastic input, and how to formulate algorithms in order for the simulation output to reflect accurately the propagation of uncertainty. Assuming we can quantify numerical accuracy, the new objective is to model uncertainty from the beginning of the simulation and not simply as an afterthought!

To this end, the Monte-Carlo approach can be employed but it is computationally expensive and it is only used as the last resort. The sensitivity method is an alternative more economical approach, based on moments of samples, but it is less robust and it depends strongly on the modelling assumptions [7]. There are other more suitable methods for physical applications, and there has already been good progress in other fields, most notably in seismology and structural mechanics. A number of papers and books have been devoted to this subject, e.g. References [8–15].

The most popular technique for modelling stochastic engineering systems is the perturbation method where all stochastic quantities are expanded around their mean via a Taylor series. This approach, however, is limited to small perturbations and does not readily provide information on high-order statistics of the response. A more effective approach pioneered by Ghanem and Spanos in the context of finite elements for solid mechanics is based on a spectral representation of the uncertainty [11]. This allows high-order representation, not just first-order as in most perturbation-based methods, at high computational efficiency. It is based on the original ideas of Wiener (1938) on Homogeneous or Polynomial Chaos (PC) and employs Hermite polynomials [16].

We will adopt this approach in the current work for representing the uncertainty spectrally, and we will perform Galerkin projections to formulate the governing equations. The resulted system of equations is a deterministic coupled set of partial differential equations, which can be solved using standard algorithms for temporal and spatial discretization. This is one of the most attractive features of this method, namely that the deterministic solvers that have already been developed can be used directly in the new context. The coupling terms include inner products involving the Hermite polynomial functionals and can be pre-computed. The Wiener–Hermite expansion is hierarchical, a sort of generalized Fourier series in the random space, and every new mode after the second-order term denotes *deviation* from the Gaussian distribution.

In the next section, we will review the main ideas of PC and apply it to a second-order linear oscillator in Section 3. In Section 4 we formulate new PC equations for the incompressible Navier–Stokes equations and present an application to flow-structure interactions. We conclude with a discussion of open issues in PC applied to non-linear problems and large domains and present possible extensions to a broader set of random distributions.

2. REPRESENTATION OF RANDOM PROCESSES

In this section, we briefly review the PC expansion, along with another important technique for representating a random process, namely the Karhunen–Loeve (KL) expansion. The KL

expansion is useful especially for decomposing the input random processes. Throughout this paper, we will use the symbol $\boldsymbol{\xi}$ to denote the standard Gaussian random variable, i.e. Gaussian random variable with zero mean and unit variance.

2.1. Polynomial Chaos expansion

The PC expansion was first proposed by Wiener [16]. According to the theorem by Cameron and Martin [17], it converges to any functional of L_2 in the L_2 sense. Thus, PC provides a means for expanding second-order random processes in terms of orthogonal polynomials. Second-order random processes refer to the processes with finite variance, or from a physical point of view, processes with finite 'energy'. Thus, a second-order random variable $X(\theta)$, viewed as a function of θ (the independent random parameter), can be represented in the form

$$\begin{aligned} X(\theta) = a_0 H_0 &+ \sum_{i_1=1}^{\infty} a_{i_1} H_1(\xi_{i_1}(\theta)) \\ &+ \sum_{i_1=1}^{\infty} \sum_{i_2=1}^{i_1} a_{i_1 i_2} H_2(\xi_{i_1}(\theta), \xi_{i_2}(\theta)) \\ &+ \sum_{i_1=1}^{\infty} \sum_{i_2=1}^{i_1} \sum_{i_3=1}^{i_2} a_{i_1 i_2 i_3} H_3(\xi_{i_1}(\theta), \xi_{i_2}(\theta), \xi_{i_3}(\theta)) \\ &+ \cdots \end{aligned} \tag{1}$$

where $H_n(\xi_{i_1}, \ldots, \xi_{i_n})$ denotes the PC of order n in the Gaussian random variables $(\xi_{i_1}, \ldots, \xi_{i_n})$. The above equation is the discrete version of the original Wiener–Hermite expansion, where the continuous integrals are replaced by summations. The expression of the Hermite polynomials H_n is given by

$$H_n(\xi_{i_1}, \ldots, \xi_{i_n}) = \mathrm{e}^{(1/2)\boldsymbol{\xi}^{\mathrm{T}}\boldsymbol{\xi}} (-1)^n \frac{\partial^n}{\partial \xi_{i_1} \cdots \partial \xi_{i_n}} \mathrm{e}^{-(1/2)\boldsymbol{\xi}^{\mathrm{T}}\boldsymbol{\xi}} \tag{2}$$

where $\boldsymbol{\xi}$ denotes the vector consisting of n Gaussian random variables $(\xi_{i_1}, \ldots, \xi_{i_n})$. For notational convenience, Equation (1) can be rewritten as

$$X(\theta) = \sum_{j=0}^{\infty} \hat{a}_j \Psi_j(\boldsymbol{\xi}) \tag{3}$$

where the functionals $\Psi_j(\boldsymbol{\xi})$ are simply a re-ordering of $H_n(\xi_{i_1}, \ldots, \xi_{i_n})$ PC forms a complete orthonormal basis in the L_2 space of random variables $\boldsymbol{\xi}$, i.e.

$$\langle \Psi_i \Psi_j \rangle = \langle \Psi_i^2 \rangle \delta_{ij} \tag{4}$$

where δ_{ij} is the Kronecker delta and $\langle \cdot, \cdot \rangle$ denotes the ensemble average, i.e. the inner product in the Hilbert space of random variables:

$$\langle f(\boldsymbol{\xi}) g(\boldsymbol{\xi}) \rangle = \int f(\boldsymbol{\xi}) g(\boldsymbol{\xi}) W(\boldsymbol{\xi}) \, \mathrm{d}\boldsymbol{\xi} \tag{5}$$

where the weighting function is

$$W(\boldsymbol{\xi}) = \frac{1}{\sqrt{(2\pi)^n}} \mathrm{e}^{-(1/2)\boldsymbol{\xi}^{\mathrm{T}}\boldsymbol{\xi}} \tag{6}$$

What distinguishes the PC expansion from other possible complete sets of expansions is that the Hermite polynomials here are orthonormal with respect to the weighting function $W(\boldsymbol{\xi})$ that has the form of a n-dimensional independent Gaussian probability distribution with unit variance. We list the one-dimensional polynomials for demonstration purpose. When $n = 1$, the polynomials are as follows:

$$\Psi_0 = 1, \quad \Psi_1 = \xi, \quad \Psi_2 = \xi^2 - 1, \quad \Psi_3 = \xi^3 - 3\xi, \quad \ldots \tag{7}$$

The orthogonality condition takes the form

$$\langle \Psi_i \Psi_j \rangle = \langle \Psi_i^2 \rangle \delta_{ij} = (i!)\delta_{ij} \tag{8}$$

2.2. Karhunen–Loeve expansion

The Karhunen–Loeve expansion [18] is another way of representing a random process [18]. It is based on the spectral expansion of the covariance function of the process. Let us denote the process as $h(t, \theta)$ and its covariance function as $R_{hh}(t_1, t_2)$, where t_1 and t_2 are the two temporal co-ordinates. By definition, the covariance function is real, symmetric and positive definite. It has an orthogonal set of eigenfunctions which forms a complete basis. The KL expansion then takes the following form:

$$h(t, \theta) = \bar{h}(t) + \sum_{i=1}^{\infty} \sqrt{\lambda_i} \phi_i(t) \xi_i(\theta) \tag{9}$$

where $\bar{h}(t)$ denotes the mean of the random process and $\xi_i(\theta)$ is a set of independent random variables. Also, $\phi_i(t)$ and λ_i are the set of eigenfunctions and eigenvalues of the covariance function, respectively, i.e.

$$\int R_{hh}(t_1, t_2) \phi_i(t_2) \, \mathrm{d}t_2 = \lambda_i \phi_i(t_1) \tag{10}$$

If the random process itself $h(t, \theta)$ is a Gaussian process, then the random variables ξ_i form an orthonormal Gaussian vector. Among many possible decompositions of a random process, the KL expansion is optimal in the sense that the mean-square error resulting from a finite-term representation of the process is minimized [11]. Its use is limited as the covariance function of the solution process is often not known *a priori*. Nevertheless, the KL expansion still provides a powerful means for representating the input random processes when the covariance structure is known.

3. STOCHASTIC SECOND-ORDER OSCILLATOR

For demonstration purposes, we will first apply the PC method to a damped linear oscillator subject to a random external forcing $f(t)$ of the form

$$\ddot{x}(t) + c\dot{x}(t) + kx(t) = f(t), \quad x(0) = x_0 \quad \text{and} \quad \dot{x}(0) = \dot{x}_0, \quad t \in [0, T] \tag{11}$$

Equation (11) has been normalized with respect to the mass, and thus the forcing $f(t)$ has units of acceleration. Also, the damping factor c and spring factor k are defined as follows:

$$c = 2\zeta\omega_0 \quad \text{and} \quad k = \omega_0^2 \tag{12}$$

where ζ and ω_0 are the damping ratio and the natural frequency of the system, respectively. This system becomes stochastic if the external forcing or the input parameters or both are random quantities. Those random quantities can evolve in time (random process) or not (random variable). In the present work, we consider the case of the response of the system subject to a Gaussian random external excitation with correlated disturbances in time (random process case). The input process is assumed to be a weakly stationary random process, with zero mean and correlation function $R_{ff}(\tau)$, applied over a time interval $[0, T]$. We can rewrite Equation (11) as

$$\ddot{x}(t) + 2\zeta\omega_0\dot{x}(t) + \omega_0^2 x(t) = f(t,\theta), \quad x(0) = x_0 \quad \text{and} \quad \dot{x}(0) = \dot{x}_0, \quad t \in [0,T] \tag{13}$$

Specifically, we choose the random input to be a first-order Markov process and it is determined by its correlation function:

$$R_{ff}(\tau) = \sigma_f^2 \mathrm{e}^{-|\tau|/A}, \quad A > 0 \tag{14}$$

where A is the correlation length, and σ_f denotes the standard deviation of the process. It can be verified that $f(t,\theta)$ is the stationary solution of the differential equation:

$$\dot{f}(t) = -\frac{1}{A} f(t) + \sigma_f \sqrt{\frac{2}{A}} W(t) \tag{15}$$

in which $W(t)$ is the zero-mean stationary white noise with covariance function $\delta(t)$.

Knowing the initial state of the system, there exists a theoretical solution for the steady-state covariance matrix

$$\Gamma = \lim_{t\to\infty} \Gamma(t)$$

of the solution of the system see Reference [19]. This solution is obtained assuming that $\Gamma(0) = \Gamma_0 = 0$. In particular, we have

$$\Gamma_{xx} = \left(\frac{2\zeta\omega_0 + 1/A}{2\zeta\omega_0^3}\right)\left(\frac{\sigma_f^2}{\omega_0^2 + (1/A)^2 + 2\zeta\omega_0/A}\right) \tag{16}$$

Given the correlation function of the input in the time domain, we employ the Karhunen–Loeve expansion to decompose the random input process. The corresponding eigenvalue problem is solved analytically. The eigenvalues and eigenfunctions are as follows:

$$\lambda_i = \frac{2/A}{(1/A)^2 + \omega_i^2} \quad \text{and} \quad f_i(t) = \alpha\left(\cos(\omega_i t) + \frac{1}{A\omega_i}\sin(\omega_i t)\right), \quad i = 1, 2, \ldots, n \tag{17}$$

where

$$\alpha = \left\{\frac{1}{2}\left(T\left(1 + \left(\frac{1}{A\omega_i}\right)^2\right) + \frac{\sin(2\omega_i T)}{2\omega_i}\left(1 - \left(\frac{1}{A\omega_i}\right)^2\right) - \frac{1}{A\omega_i^2}(\cos(2\omega_i T) - 1)\right)\right\}^{-1/2} \tag{18}$$

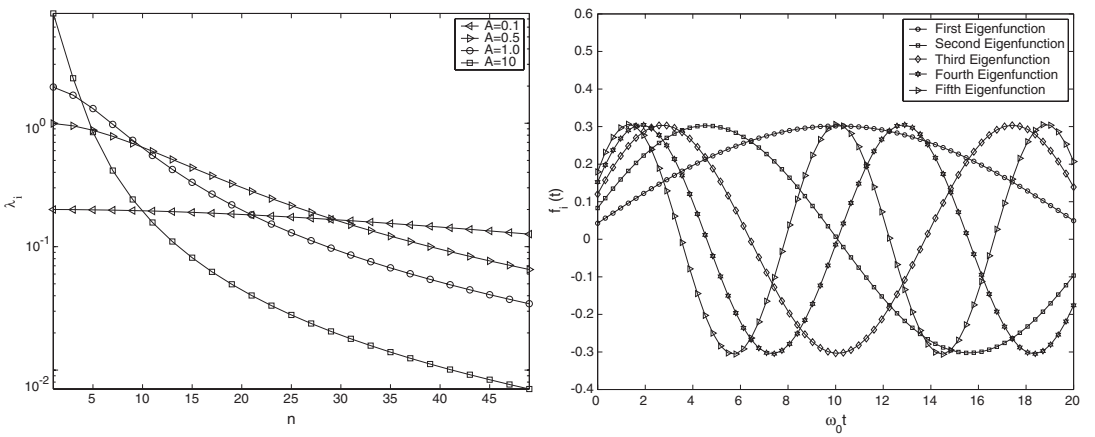

Figure 2. Eigenvalues λ_i for various values of the correlation length A. $T = 20$ (left). Eigenfunctions $\phi_i(t)$, $t \in [0, T]$, $n = 1, 2, 3, 4, 5$ and correlation length $A = 1$. $T = 20$ (right).

The normalization coefficient α ensures that $\int_0^T f_i^2(t)\,\mathrm{d}t = 1$. Here, A is the correlation length, $[0, T]$ is the size of the time domain, and ω_i are determined numerically by solving:

$$\left(\omega_i^2 - \left(\frac{1}{A}\right)^2\right)\tan(\omega_i T) - 2\frac{\omega_i}{A} = 0, \quad i = 1, 2, \ldots, n \tag{19}$$

For a given correlation length A and a standard deviation σ_f of the random process $f(t, \theta)$, we decompose the input in its truncated Karhunen–Loeve expansion up to the random dimension n, i.e.

$$f(t, \theta) = \bar{f}(t) + \sigma_f \sum_{i=1}^{n} \sqrt{\lambda_i}\phi_i(t)\xi_i(\theta) \tag{20}$$

The number of terms, i.e. random dimension n, needs to be large enough in order to resolve the scales associated with the correlation length A. Plots of eigenvalues and eigenfunctions are shown in Figure 2. In this case, the damping and spring factors are taken equal to 1, the mean $\bar{f}$ of the external forcing f is equal to 0 and its standard deviation is $\sigma_f = \sqrt{3}$. We note that the smaller the value of the correlation length A the higher is the contribution from terms with small eigenvalues.

The solution of the problem is sought in the form given by its truncated PC expansion:

$$x(t, \theta) = \sum_{j=0}^{P} x_j(t)\Phi_j(\xi(\theta)) \tag{21}$$

with

$$P = \frac{(n + p)!}{n!\,p!} - 1 \tag{22}$$

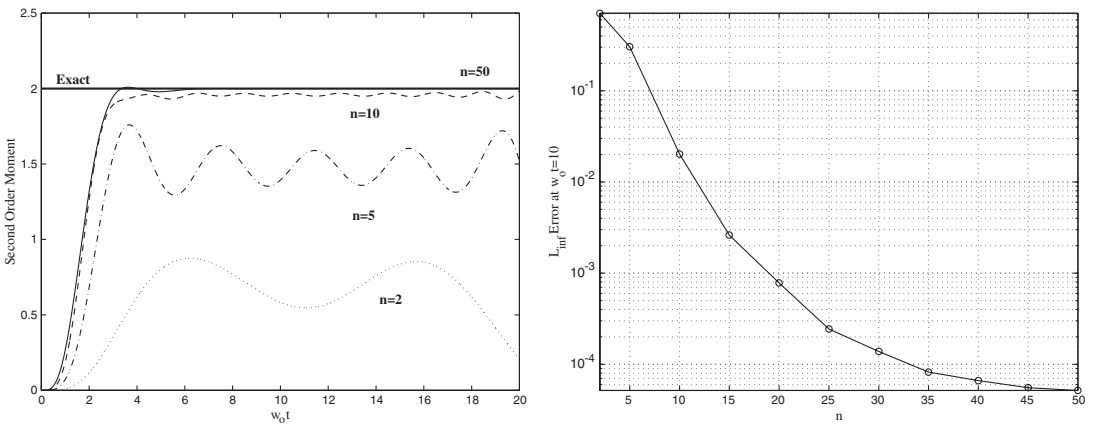

Figure 3. Time evolution of second-order moment Γ_{xx} for different number of random dimensions n (left). Convergence rate of second-order moment Γ_{xx} versus the number of random dimensions n (right).

where n is the number of random dimensions and p is the highest polynomial order of the PC expansion.

To formulate the algebraic equations, we first expand the right-hand side of Equation (13) in its Karhunen–Loeve series and we also expand the response process $x(t)$ in its PC series (see Equation (21)). The system does not exhibit any non-linearity in random space because only the right-hand side of Equation (13) is random. This implies that quadratic or higher-order terms in the PC expansion will not improve the accuracy of the solution. Therefore, we use only *linear terms* in the expansion which means that we take a constant value of $p=1$ in Equation (22). We then study the effect of the number of dimensions n in the expansion. The algebraic system is obtained by a Galerkin projection of the discretized Equation (13), and standard deterministic solvers are employed for the solution [20]. This is so because the Galerkin projection takes advantage of the orthogonality of the basis so all randomness, which is represented in the basis, is eliminated giving rise to a deterministic system. This, in fact, is a key to the efficiency and accuracy of the method. Most numerical methods for stochastic differential equations are first-order due to lack of regularity in the solution. In contrast, the PC method can be of arbitrarily high-order depending on the solver involved.

We compute the second-order moment of the solution for different values of the random dimensions n and for a correlation length $A=1.0$. We examine its evolution versus non-dimensional time $\tau=\omega_0 t$ as shown in Figure 3 (left). For the chosen set of parameters, the theoretical value of the *variance* of the solution as $t\to\infty$ is 2, shown on the figure by the solid black line. We see that as the number n increases the numerical solution converges asymptotically to the theoretical solution. We then compare the L_∞ error at time $t=10$ of the numerical solution versus the exact solution, as shown Figure 3 (right). We examine the decaying of this error versus the number of terms n in the Karhunen–Loeve expansion. Similar to the decay rate of the eigenvalues in Figure 2 (left), here we see that the error initially decays exponentially (for $n<15$) but eventually saturates (for $15<n<50$) as we reach a large number of random dimensions.

The linear problem we have considered here driven by *nearly* white noise is in some sense a very difficult problem for PC and represents an extreme case. The solution accuracy is totally determined by the input dimensionality barring any numerical integration errors. However, in many CFD problems the stochastic input is sufficiently represented by a much smaller number of dimensions, e.g. $n = 2$–4 but non-linearities require that a high-order Wiener–Hermite polynomial be employed, i.e. $p > 1$ to capture non-Gaussian effects. We will demonstrate this in the next section where we deal with the full Navier–Stokes equations.

4. INCOMPRESSIBLE NAVIER–STOKES EQUATIONS

We consider the incompressible Navier–Stokes equations

$$\nabla \cdot \mathbf{u} = 0 \tag{23}$$

$$\frac{\partial \mathbf{u}}{\partial t} + \mathbf{u} \cdot \nabla \mathbf{u} = -\nabla \Pi + Re^{-1} \nabla^2 \mathbf{u} \tag{24}$$

where Π is the pressure and Re is the Reynolds number of the flow. The flow can behave randomly subject to the randomness imposed from either initial conditions or boundary conditions (or both). Even in the case where both initial and boundary conditions are deterministic, stochastic solution can still be obtained due to the intrinsic non-linearity of the Navier–Stokes equations (e.g. turbulence flow) but here we will consider laminar flow at relatively low Reynolds number.

We expand the velocity and pressure in terms of PC, i.e.

$$\mathbf{u}(\mathbf{x}, t, \theta) = \sum_{i=0}^{P} \mathbf{u}_i(\mathbf{x}, t) \Psi_i(\xi(\theta)) \tag{25}$$

$$\Pi(\mathbf{x}, t, \theta) = \sum_{i=0}^{P} \Pi_i(\mathbf{x}, t) \Psi_i(\xi(\theta)) \tag{26}$$

We then substitute the PC expansions into Navier–Stokes Equations (23) and (24) and we project the obtained equations onto the random space spanned by the basis polynomials $\{\Psi_i\}$ by taking the inner product with each basis and using the orthogonality condition (8). We obtain the following discrete set of deterministic equations:

For $k \in [0, P]$

$$\nabla \cdot \mathbf{u}_k = 0 \tag{27}$$

$$\frac{\partial \mathbf{u}_k}{\partial t} + \frac{1}{\langle \Psi_k^2 \rangle} \sum_{i=0}^{P} \sum_{j=0}^{P} e_{ijk} (\mathbf{u}_i \cdot \nabla) \mathbf{u}_j = -\nabla \Pi_k + Re^{-1} \nabla^2 \mathbf{u}_k \tag{28}$$

where $e_{ijk} = \langle \Psi_i \Psi_j \Psi_k \rangle$.

The above set of $(P+1)$ 'Navier–Stokes-like' equations for each random mode is only coupled through the convective terms, for details see Reference [21].

4.1. Numerical implementation

Discretization in space and time can be carried out by any conventional method. We use the spectral/*hp* element method in space in order to have a better control of the numerical error coming from the deterministic component [22]. The high-order splitting scheme together with properly defined consistent pressure boundary conditions are imployed in time [23]. In particular, the spatial discretization is based on Jacobi polynomials on triangles or quadrilaterals in two-dimensions, and tetrahedra, hexahedra or prisms in three-dimensions.

Once we have obtained the coefficients in the expansion of the solution (see Equations (25) and (26)), we have an analytical form of the solution process. The *mean* of the solution is contained in the expansion term with index of zero. The second-order moment of the solution (velocity or pressure field), i.e. the covariance function is given by

$$\begin{aligned} R_{uu}(\mathbf{x}_1,t_1;\mathbf{x}_2,t_2) &= \langle u(\mathbf{x}_1,t_1)-\overline{u(\mathbf{x}_1,t_1)}, u(\mathbf{x}_2,t_2)-\overline{u(\mathbf{x}_2,t_2)}\rangle \\ &= \sum_{i=1}^{P} [u_i(\mathbf{x}_1,t_1)u_i(\mathbf{x}_2,t_2)\langle\Psi_i^2\rangle] \end{aligned} \tag{29}$$

The variance of the solution is obtained as

$$\begin{aligned} \mathrm{Var}(u(\mathbf{x},t)) &= \langle (u(\mathbf{x},t)-\overline{u(\mathbf{x},t)})^2\rangle \\ &= \sum_{i=1}^{P} [u_i^2(\mathbf{x},t)\langle\Psi_i^2\rangle] \end{aligned} \tag{30}$$

and the root-mean-square (rms) is the square root of the variance.

4.2. Application to flow-structure interactions

We consider two-dimensional flow-structure interactions problems subject to stochastic inputs. In particular, we are interested in the case of an elastically mounted circular cylinder with random structural parameters, subject to vortex-induced vibrations. We study the case of an unsteady flow in the subcritical regime with $Re = Ud/\nu = 100$ (U is the free-stream velocity, d the cylinder diameter and ν is the kinematic viscosity). The flow is computed using the procedure outlined above while the structural response of the moving cylinder is computed using the procedure described in Section 3.

In this section, we assume the damping coefficient and the spring factor of the structure to be both random variables. The free structure, excited by the vortex shedding of the flow which is initially deterministic, produces a random response. Therefore, the position of the boundary of the cylinder becomes stochastic. This random boundary affects the flow domain, and consequently the flow itself becomes a stochastic process. The fluid forces on the cylinder derived from the random flow velocity field and the random pressure field are random processes as well. The damped oscillator is then subject to random parametric (random variables) and external forcing (random process) excitations.

Because the response of the cylinder to the vortex shedding is mainly in the cross-flow direction and due to the increased complexity introduced by the random character of the system, we have constrained the cylinder movement in one direction. Therefore, the cylinder is free to oscillate in the cross-flow y-direction but it is forced to have no motion in the streamwise x-direction. If we denote by $\eta = y/d$, then the governing equation for the structure is

$$\ddot{\eta}(t,\theta) + c(\theta)\dot{\eta}(t,\theta) + k(\theta)\eta(t,\theta) = \mathbf{F}(t,\theta), \quad \eta(0) = \eta_0 \quad \text{and} \quad \dot{\eta}(0) = \dot{\eta}_0 \tag{31}$$

The damping coefficient c and spring factor k are both random variables with Gaussian distributions. The forcing excitation term on the right-hand side of Equation (31) is not known *a priori* and has to be computed once the flow distribution has been obtained. This is done every timestep, with the fluid forces acting on the cylinder surface computed as follows:

$$\mathbf{F}(t,\theta) = \oint \left(-\Pi(t,\theta)\mathbf{n} + \frac{1}{Re}(\nabla \mathbf{u}(t,\theta) + \nabla \mathbf{u}(t,\theta)^{\mathrm{T}}) \cdot \mathbf{n} \right) \mathrm{d}s \tag{32}$$

where $\mathbf{n}$ is the unit normal. For the temporal discretization of Equation (31) we use the implicit, second-order Newmark scheme [20].

To simplify the solution of the flow equations, we consider the initial co-ordinate system (x', y', t') and a co-ordinate system (x, y, t) attached to the moving cylinder. This maps the time-dependent and moving problem to a stationary and non-deforming one. Specifically, we introduce the following mapping:

$$\begin{aligned} x &= x' - \zeta(t') \\ y &= y' - \eta(t') \\ t &= t' \end{aligned}$$

For a two-dimensional flow, this transformation amounts to an adjustment of u and v by the cylinder velocity:

$$\begin{aligned} u &= u' - \frac{\partial \zeta}{\partial t'} \\ v &= v' - \frac{\partial \eta}{\partial t} \\ \Pi &= \Pi' \end{aligned}$$

The Navier–Stokes and continuity equations are transformed to

$$\frac{\partial \mathbf{u}}{\partial t} + (\mathbf{u} \cdot \nabla)\mathbf{u} = -\nabla \Pi + Re^{-1}\nabla^2 \mathbf{u} + \mathbf{A}(\zeta, \eta) \tag{33}$$

$$\nabla \cdot u = 0 \tag{34}$$

where the forcing term $\mathbf{A}(\zeta, \eta)$ is the extra acceleration term introduced by the transformation. In 2D flow, with no streamwise motion of the cylinder, $A(\zeta, \eta)$ has a very simple form:

$$A_x = 0 \quad \text{and} \quad A_y = -\frac{\partial^2 \eta}{\partial t^2} \tag{35}$$

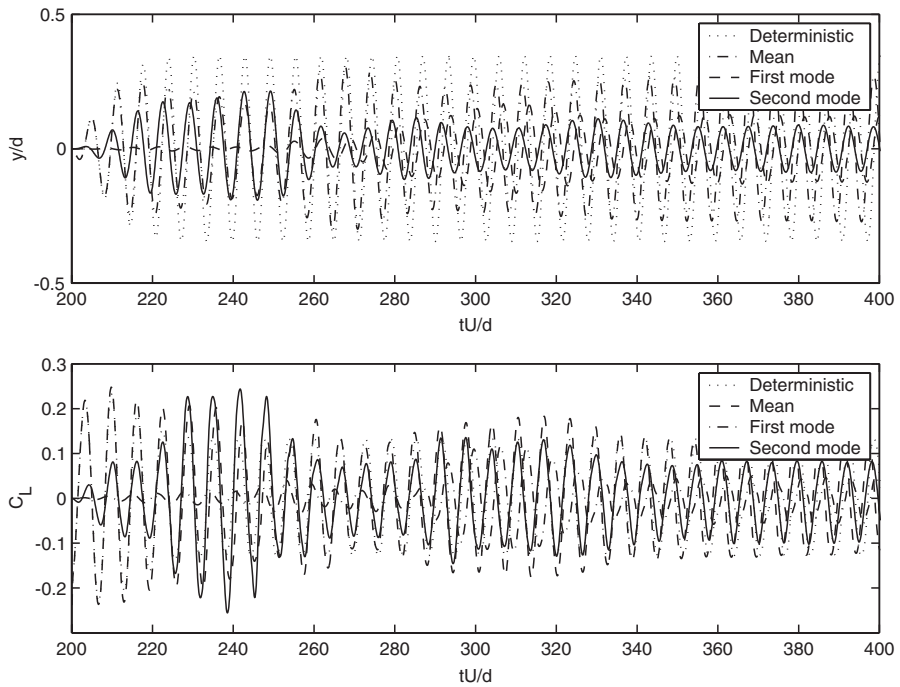

Figure 4. Time evolution of the leading random modes for the cylinder cross-flow response y/d (top) and the lift coefficient C_{L} (bottom).

Since the mapping involves the random cylinder velocity, it is a random process itself and it needs to be also represented by a chaos expansion.

4.3. Numerical results

The chosen parameters for the flow suggest that we are in the laminar flow regime. The Reynolds number is $Re = 100$, and the random parameters for the structure are set to:

- $(\bar{c}, \sigma_c) = (0.1, 0.01)$, $(\bar{k}, \sigma_k) = (1.0, 0.2)$

(see Equation (31)), while the initial conditions η_0 and $\dot{\eta}_0$ are set to 0. We note that there is a non-zero probability that the oscillator has a natural frequency $\omega_0 = \sqrt{k}$ matching the vortex shedding frequency of a fixed cylinder at this Reynolds number. Also, the system has two random dimensions ($n = 2$), and we use third-order PC expansion ($p = 3$), which corresponds to a 10-term chaos expansion (i.e. $P + 1 = 10$).

In Figure 4, we plot the time evolution of the leading random modes of the cylinder response. We show the non-dimensional cross-flow displacement y/d of the cylinder (top) and the corresponding lift coefficient $C_{\mathrm{L}} = F_y/(0.5\rho d U^2)$ (bottom; with F_y the lift force), along with the deterministic solution. As expected, the *mean* response, due to the diffusion effect of the randomness, has a smaller amplitude than the deterministic solution. The first

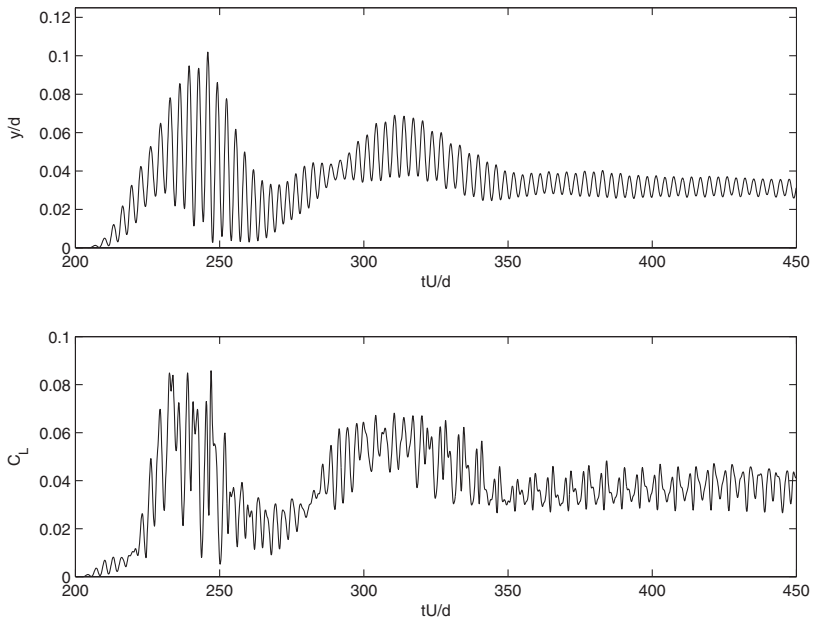

Figure 5. Time evolution of the *variance* of the structural solution. Variance of the cylinder cross-flow response y/d (top) and variance of the lift coefficient C_L (bottom).

and second modes represent the Gaussian part of the solution. In Figure 5, we show the time evolution of the *variances* of the non-dimensional cross-flow displacement y/d (top) and the corresponding lift coefficient C_L (bottom). In both cases, after an initial peak in the response, the signal eventually reaches a stationary periodic state. The initial peak value can be two times larger than that of the final periodic state. This could indicate that as the randomness propagates from the cylinder body to the flow domain downstream, some strong interactions and possibly unstable phenomena take place. It is, therefore, important that the stochastic simulation be sufficiently robust to be able to capture accurately this initial transient regime.

Figure 6 shows instantaneous flood contours (grey scale) and contour lines (white colour) of *rms* and *mean* of cross-flow velocity, respectively. Figure 7 shows the same kind of plot for the vorticity field. Both snapshots are taken at $t = 600$ (non-dimensional time units) corresponding to more than 100 shedding cycles from the beginning of the simulation. Regions of the flow domain with high uncertainty are the shear layers and the near-wake of the cylinder, which are of course the regions of utmost physical interest!

Figure 6 suggests that the *rms* values of cross-flow velocity are not strongly spatially correlated to the mean values; for example the contours with the largest values are not aligned. In the near-wake up to $x/d = 7.0$, large variance is obtained at the boundary between flow structures of mean, but further downstream, as the system reaches equilibrium, large variance realigns with large values of the mean. Figure 7 shows this more consistently along the wake, where there is a strong correlation between variance and mean values of the vorticity. Large variance of the vorticity is obtained in the regions of large shear or strong mean vorticity.

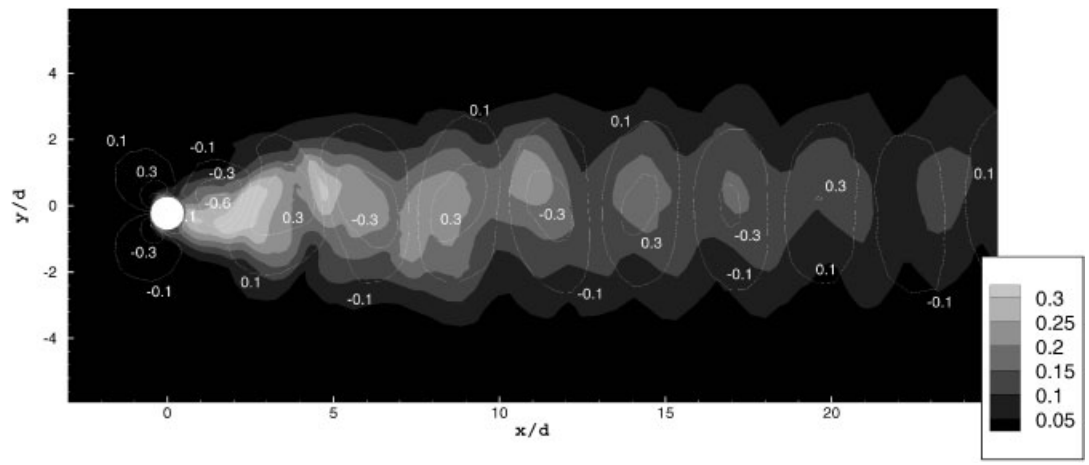

Figure 6. Instantaneous spatial distribution of *rms* (grey scale) and *mean* (white line) of cross-flow velocity.

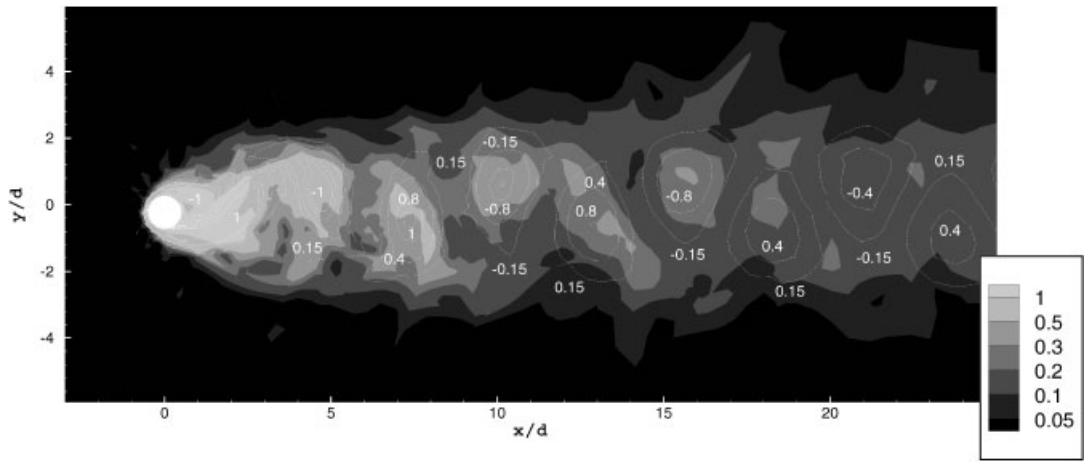

Figure 7. Instantaneous spatial distribution of *rms* (grey scale) and *mean* (white line) of vorticity.

Figure 8 presents the pressure distribution on the cylinder surface at different instants within one shedding cycle. The figure shows four different instants, from non-dimensional time $t_0 = 602.4$ (top left plot) to $t_0 + 3T/4$ (bottom right plot) within one shedding cycle of period T. Each plot shows an instantaneous polar view of the pressure distribution on the cylinder surface as well as the mean cross-flow position of the cylinder y/d at the corresponding time. The cylinder is represented by a black disk. The flow orientation is from left to right in each plot. Therefore, the angle $\theta = 180^\circ$ on the polar view corresponds to the

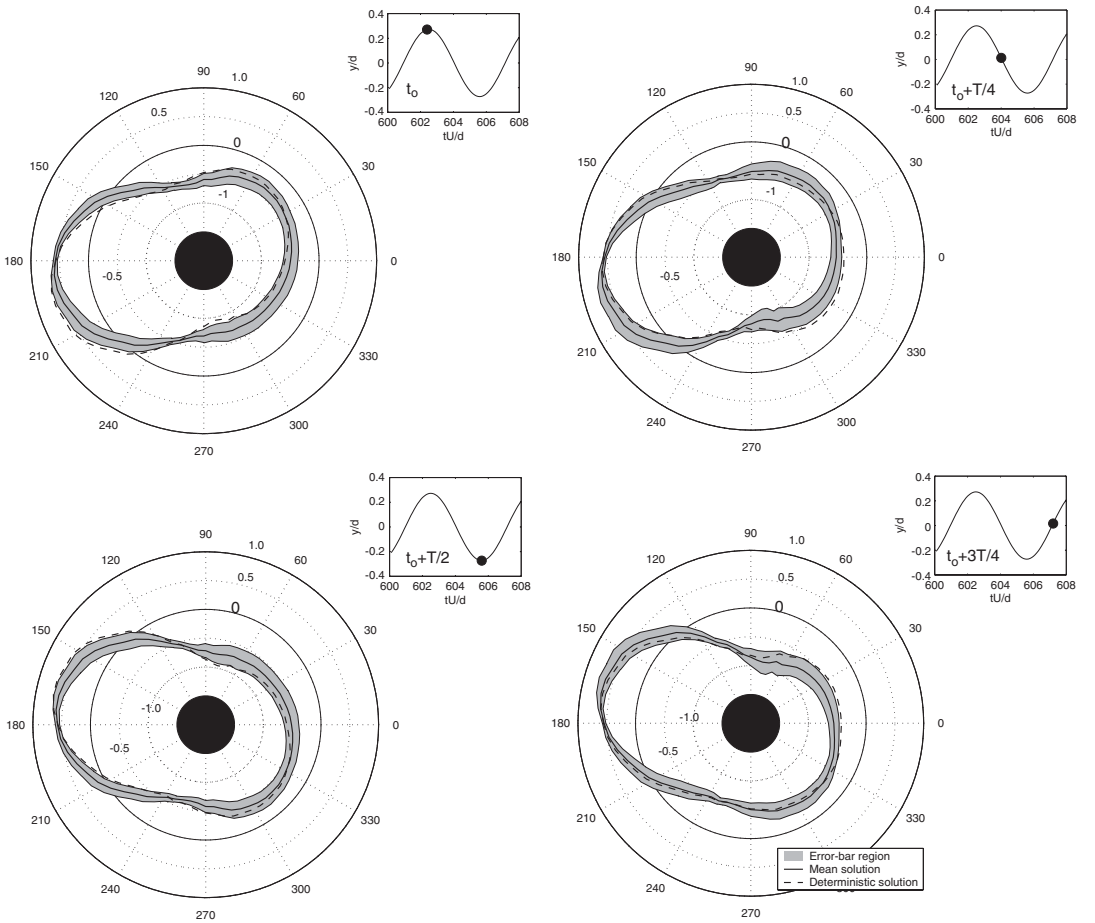

Figure 8. Polar plots of pressure distribution on the cylinder surface relative to the cylinder *mean* cross-flow position at four different instants within one shedding cycle. Deterministic pressure solution (dashed line); Stochastic pressure solution (solid line and shaded area).

front stagnation point and $\theta = 0^\circ$ corresponds to the rear stagnation point. Successive dashed circles give pressure value levels (the zero value is a solid circle). The deterministic pressure solution is represented by a dashed line while the stochastic solution is represented by a solid line (mean pressure solution) and a shaded area ('*error-bar*' region of the pressure solution). This region is centred around the mean curve and its span is two standard deviations (i.e. one *std* above and one *std* below the mean value). Pressure values are mainly in the range from -1.0 to 1.0, and both deterministic and stochastic pressure solutions take positive values around the front stagnation point. Noticeable differences exist between stochastic and deterministic solutions. In particular, temporal as well as spatial changes in the pressure variance (or '*error-bar*' region) can be seen. However, the deterministic signal remains, most of the time, inside the envelope of the stochastic solution. Small uncertainty (in terms of Gaussian

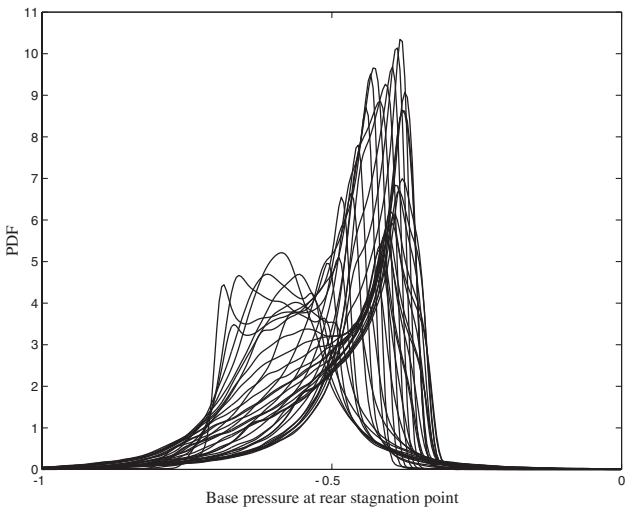

Figure 9. Probability distribution function for the pressure at the rear stagnation point at different instants within a shedding cycle.

response) is obtained at the front stagnation point and at two points close to separation on both sides of the cylinder. Values of the *std* at those locations are small and mean solutions are equivalent to the deterministic solutions. The polar angular position of these two nodes is always in the range $\theta \in [90°, 120°]$ or in the range $\theta \in [240°, 270°]$. It would be interesting to investigate the relationship between these nodes and the separation points on the cylinder.

Having obtained all the random modes, we can now reconstruct the solution and examine its probability distribution function (PDF) at different times within a shedding cycle. Figures 9 and 10 show the PDFs of the pressure at the rear stagnation point and of the crossflow amplitude of oscillation at different time instants. It is clear that the PDF of the amplitude of the cylinder oscillation is symmetric, as expected, but the PDF of the base pressure shows a strong bias towards one side.

In Figures 11 and 12 we plot the time evolution of the base pressure and of the cylinder amplitude of cross-flow oscillation. Also shown are error bars at five time instants and corresponding probability distribution functions. There is a large difference of the deterministic versus the *mean* stochastic solution as a function of time. Specifically, for the cylinder oscillation the amplitude PDF approaches a 'lognormal' form on the left side, it transitions through a uniform-like distribution (between time IV and time V), and finally reverses to the other side resembling a lognormal distribution again. It is also interesting to observe that the PDF with the sharp left side (time II) occurs when the cylinder has maximum negative displacement in this case. Often, smaller variance occurs when the displacement is close to its maximum value as opposed to when it is closed to some 'average' value. Here, the left side of the PDF of time II is very sharp, which means that the cylinder has almost 'no chance' to go any lower down (because it reaches its minimum value) but it will most likely go back up.

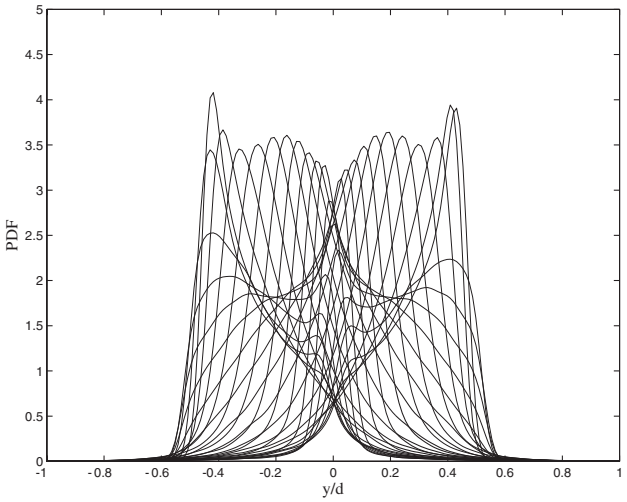

Figure 10. Probability distribution function for the amplitude of the crossflow oscillation at different instants within a shedding cycle.

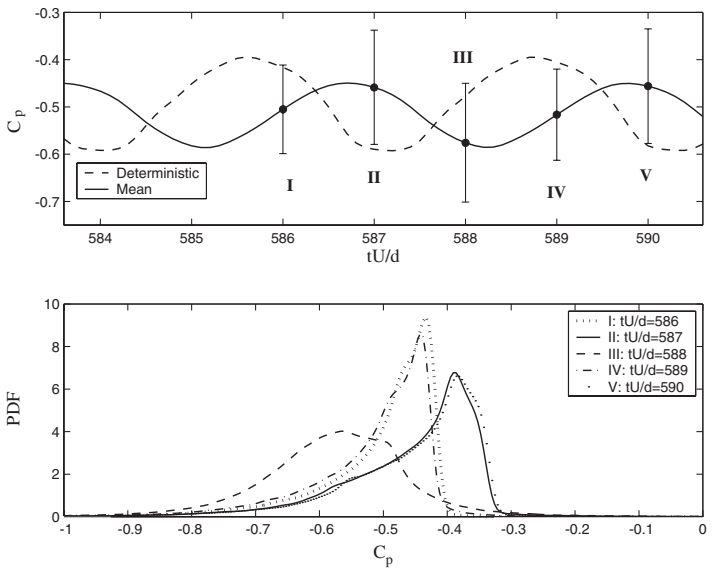

Figure 11. Upper: Time variation of the *mean* base pressure (with error bars) versus the *deterministic solution*. Lower: Probability distribution function of base pressure at five time instants marked in the top plot.

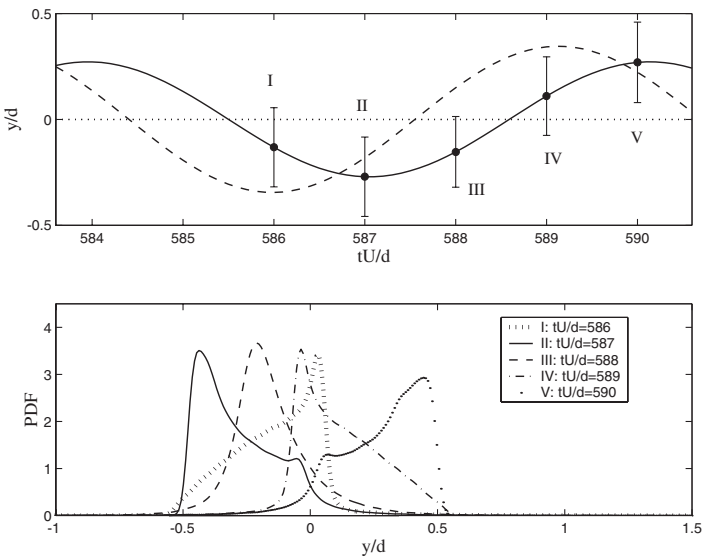

Figure 12. Upper: Time variation of the *mean* amplitude of cylinder oscillation (with error bars) versus the *deterministic solution*. Lower: Probability distribution function of amplitude at five time instants marked in the top plot.

5. OPEN ISSUES IN POLYNOMIAL CHAOS

5.1. Resolution properties of Wiener–Hermite expansions

PC is perhaps the most efficient approach for simulating uncertainties in flow problems, with observed speed-up factors from 1000 to more than 100 000 compared to Monte Carlo simulation, depending on the problem. For flows with *time-dependent mean* it is particularly effective and does not require constructing careful ensemble averages as in other probabilistic approaches. The above speed-up estimate applies to stochastic input which is at least *partially correlated* and its dimensionality is relatively low. However, for a random process describing an input with a very short correlation length, a high dimensional chaos expansion is required. As shown in Equation (22), the number of expansion terms $(P+1)$ increases fast, although algebraically, both with the dimension n as well as the polynomial order p. Therefore, processes involving *nearly white noise*, like the second-order oscillator example presented in Section 3, are particularly difficult to handle with PC.

The effectiveness of Hermite expansions has been recognized long ago, and Chorin [24] employed Wiener–Hermite series to substantially improve both accuracy and computational efficiency of Monte-Carlo algorithms. However, the limitation of prematurely truncated Wiener–Hermite expansions in applications of turbulence was also recognized. Specifically, in the pre-DNS era Orszag and Bissonnette [25] among others examined the possibility of using Wiener–Hermite functional expansions to simulate turbulence [25]. However, they demonstrated that for a relatively simple system of three interacting modes, PC failed to reproduce the exact dynamics in equilibrium.

Although the aforementioned example is a special case of inviscid dynamics, it is representative of some of the problems that the Wiener–Hermite expansions have. The root of this problem can be attributed to the relatively poor resolution properties of Hermite expansions compared to other spectral polynomials. This has been recognized in deterministic expansions [26, 27] and re-scaling procedures have been introduced, e.g. see Reference [28], to deal with this. We explain this behaviour for the Hermite and Laguerre polynomials in the following analysis, and subsequently present a generalized PC approach.

Let us consider the expansion of the exponential function in terms of *Hermite* polynomials, i.e.

$$S \equiv \mathrm{e}^{\sigma\xi t} = \mathrm{e}^{(\sigma t)^2/2} \sum_{n=0}^{\infty} \frac{(\sigma t)^n}{n!} H_n(\xi) \tag{36}$$

To study the rate of convergence of this expansion we consider the norm

$$\|S\|^2 = (\sqrt{2\pi})^{-1} \int_{-\infty}^{\infty} \mathrm{e}^{-\xi^2/2} S^2 \, \mathrm{d}\xi = \mathrm{e}^{2\sigma^2 t^2}$$

We also denote by S_P the truncation expansion in Equation (36) that involves the first $(P+1)$ Hermite polynomials. We note here that S_P is not exactly the PC expansion but we will use it to obtain an approximate estimate. To this end, we compute

$$\|S - S_P\|^2 = \mathrm{e}^{(\sigma t)^2} \sum_{n=P+1}^{\infty} \frac{(\sigma t)^{(2n)}}{n!}$$

and thus we can estimate the relative error from

$$\frac{\|S - S_P\|^2}{\|S\|^2} = \mathrm{e}^{-(\sigma t)^2} \sum_{n=P+1}^{\infty} \frac{(\sigma t)^{(2n)}}{n!} \leqslant \mathrm{e}^{-(\sigma t)^2} \frac{(\sigma^2 t^2)^{P+1}}{(P+1)!} \frac{1}{1 - (\sigma t)^2/(P+1)}$$

where we have assumed that $(\sigma t)^2/(P+1) < 1$. In order to estimate the number of required Hermite functionals from the above inequality we introduce an error level ε so that

$$\frac{\|S - S_P\|}{\|S\|} \leqslant \varepsilon$$

In addition, we can use the PC expansion directly to compute the approximation error or inversely the number of required modes for given level of error ε. In Figure 13 we plot the two estimates versus the product (σt) for $\varepsilon = 10^{-6}$. Clearly, for long times a very large number of modes is required to maintain the error level at the prescribed level. Also, we see that the theoretical estimate provides a lower bound, i.e. it gives the least number of required modes to achieve the error level ε.

5.2. *Generalized polynomial chaos*

In this section, we briefly describe the extension of PC to representations of an input given by an arbitrarily random distribution; more details can be found in References [20, 21, 29]. The main idea is to replace the Hermite functionals with other orthogonal functionals that best describe the input. To this end, the Askey family offers a wide class of suitable continuous and

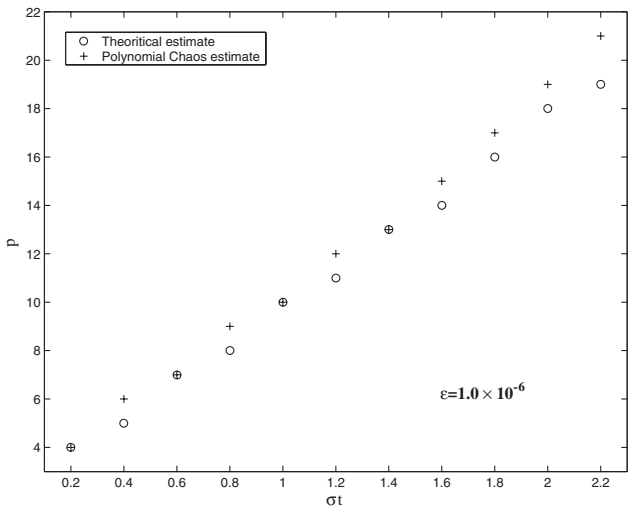

Figure 13. Estimate of required number of Hermite functionals versus the product of standard deviation with time. The circle symbols correspond to the theoretical estimate and the cross symbols correspond to the PC estimate.

Table I. Correspondence between Askey polynomial functionals and different types of random input ($N \geqslant 0$ is a finite integer).

	Random inputs	Wiener–Askey Chaos	Support
Continuous	Gaussian	Hermite-Chaos	$(-\infty, \infty)$
	Gamma	Laguerre-Chaos	$[0, \infty)$
	Beta	Jacobi-Chaos	$[a, b]$
	Uniform	Legendre-Chaos	$[a, b]$
Discrete	Poisson	Charlier-Chaos	$\{0, 1, 2, \ldots\}$
	Binomial	Krawtchouk-Chaos	$\{0, 1, \ldots, N\}$
	Negative Binomial	Meixner-Chaos	$\{0, 1, 2, \ldots\}$
	Hypergeometric	Hahn-Chaos	$\{0, 1, \ldots, N\}$

discrete polynomials [30]. Specifically, these Askey orthogonal polynomials have weighting functions the same as the probability function of certain types of random distributions. In practice, we then choose the type of independent variables $\boldsymbol{\xi}$ in the polynomials $\{\Psi_i(\boldsymbol{\xi})\}$ according to the type of random distributions as shown in Table I.

It is clear that the original Wiener polynomial chaos corresponds to the Hermite-Chaos and is a subset of the Wiener–Askey polynomial chaos. The Hermite-, Laguerre- and Jacobi-Chaos are continuous chaos, while Charlier-, Meixner-, Krawtchouk- and Hahn-Chaos are discrete chaos. It is worthy mentioning that the Legendre polynomials, which is a special case of the Jacobi polynomials, correspond to an important distribution—the *uniform distribution*. Due to the importance of the uniform distribution, we list it separately in the table and term the corresponding chaos expansion as the Legendre-Chaos.

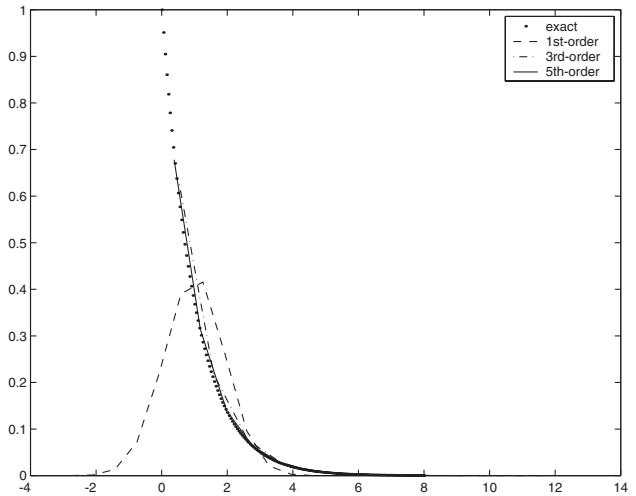

Figure 14. Approximation to exponential distribution using different orders of Wiener–Hermite Chaos.

In the following, we show what is the gain of using these new polynomials instead of the Hermite expansions. First, we consider the Gamma distribution for the specific case of $\alpha = 0$ and assume that a variable k is random following an exponential distribution with PDF of the form:

$$f(k) = \mathrm{e}^{-k}, \quad k > 0 \tag{37}$$

In Figure 14 we show the result of the approximation of the exponential distribution by the Hermite-Chaos. The PDF of different orders of the approximations are shown on the figure, together with the exact PDF of the exponential distribution. We notice that the third-order approximation gives fairly good results and fifth-order Hermite-Chaos is close to the exact distribution. The Hermite-Chaos does not approximate the PDF well at $x \sim 0$ where the PDF reaches its peak at 1. In order to capture this rather sharp region, more Hermite-Chaos terms are needed. If the optimal Wiener–Askey chaos is chosen, in this case the Laguerre-Chaos, only one term is needed to represent k *exactly*. In solutions of differential equations, the translates into essentially a loss of fast (exponential) convergence of the Hermite-Chaos in contrast to Laguerre-Chaos [29].

Next, we assume the distribution of k is Beta distribution in the domain $[0, 1]$. Figure 15 shows the PDF of first-, third- and fifth-order Hermite-Chaos approximations to the Beta random variable; the special case of the important uniform distribution is considered. It can be seen that the Hermite-Chaos approximation converges to the exact solution as the number of expansion terms increases. Oscillations are observed near the corners of the square. This is analogous to the Gibb's phenomenon, which occurs when Fourier expansions are used to approximate functions with sharp corners. For a uniform distribution, the Hermite-Chaos does not work very well due to this stochastic Gibb's phenomenon even when more higher-order terms are added. On the other hand, the first-order Jacobi-Chaos expansion is already *exact*. In addition to the exponential convergence, the proper Wiener–Askey basis leads to dramatic lowering of dimensionality of the problem.

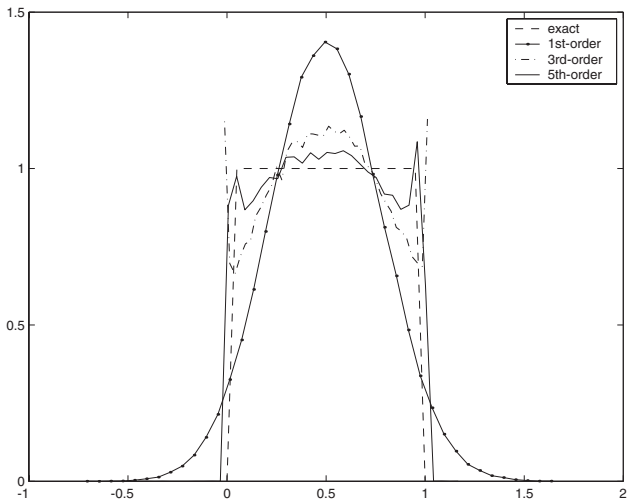

Figure 15. Approximation to uniform distribution using different orders of Wiener–Hermite Chaos.

6. SUMMARY

We have discussed in this paper the construction of error bars in CFD that reflect physical input uncertainty and its propagation in simulations. To this end, we first employed the Wiener–Hermite polynomial functionals in a second-order oscillator and a flow-structure interaction problems. Representative results obtained show that for flow simulations it is possible to quantify uncertainty both *in time* and *in space* efficiently. We have also discussed open problems associated with the Hermite polynomials and generalized PC to a wide class of Askey polynomials that best represent different types of stochastic input.

More work is needed on this front, and we believe the current paper is just the beginning of a more systematic future effort by the CFD community to incorporate statistics into simulation for more reliable answers.

ACKNOWLEDGEMENTS

This paper is based on material presented by the last author (G.K.) as keynote lecture in ECCOMAS 2001, marking the 80th birthday of Prof. O.C. Zienkiewicz. The work is sponsored by ONR and DOE, and simulations were performed at the NPACI (University of California, San Diego) and NCSA (University of Illinois, Urbana-Champaign).

REFERENCES

1. Harlow FH, Fromm JE. Computer experiments in fluid dynamics. *Scientific American* 1965; **212**(3):104–110.
2. Emmons HW. Critique of numerical modelling of fluid mechanics phenomena. *Annual Review of Fluid Mechanics* 1970; **2**:15–36.
3. Karniadakis GE, Orszag SA. Nodes, modes and flow codes. *Physics Today* 1993; **March**: 34–42.
4. Kim J, Moin P, Moser R. Turbulence statistics in fully developed channel flow at low Reynolds number. *Journal of Fluid Mechanics* 1987; **177**:133.
5. Ma X, Karamanos G-S, Karniadakis GE. Dynamics and low-dimensionality of turbulent near-wake. *Journal of Fluid Mechanics* 2000; **410**:29–65.

6. Ong L, Wallace J. The velocity field of the turbulent very near wake of a circular cylinder. *Experiments in Fluids* 1996; **40**:441–453.
7. Hills RG, Trucano TG. Statistical validation of engineering and scientific models: background. *Technical Report* SAND99-1256, Sandia National Laboratories, 1999.
8. Ghanem RG. Stochastic finite elements for heterogeneous media with multiple random non-Gaussian properties. *ASCE Journal of Engineering Mechanics* 1999; **125**(1):26–40.
9. Ghanem RG. Ingredients for a general purpose stochastic finite element formulation. *Computer Methods in Applied Mechanics and Engineering* 1999; **168**:19–34.
10. Fadale TD, Emery AF. Transient effects of uncertainties on the sensitivities of temperatures and heat fluxes using stochastic finite elements. *Journal of Heat and Mass Transfer* 1994; **116**:808–814.
11. Ghanem RG, Spanos P. *Stochastic Finite Elements: A Spectral Approach*. Springer: Berlin, 1991.
12. Liu WK, Besterfield G, Mani A. Probabilistic finite elements in nonlinear structural dynamics. *Computer Methods in Applied Mechanics and Engineering* 1986; **56**:61–81
13. Liu WK, Mani A, Belytschko T. Finite element methods in probabilistic mechanics. *Probabilistic Engineering Mechanics* 1987; **2**(4):201–213.
14. Shinozuka M, Leone E. A probabilistic model for spatial distribution of material properties. *Engineering Fracture Mechanics* 1976; **8**:217–227.
15. Shinozuka M. Structural response variability. *Journal of Engineering Mechanics* 1987; **113**(6):825–842.
16. Wiener N. The homogeneous chaos. *American Journal of Mathematics* 1938; **60**:897–936.
17. Cameron RH, Martin WT. The orthogonal development of nonlinear functionals in series of Fourier–Hermite functionals. *Annals of Mathematics* 1947; **48**:385.
18. Loève M. *Probability Theory* (4th edn). Springer: Berlin, 1977.
19. Soong TT, Grigoriu M. *Random Vibration of Mechanical and Structural Systems*. Prentice-Hall, Inc.: Englewood Cliffs, NJ, 1993.
20. Lucor D. Generalized polynomial chaos: applications to random oscillators and flow-structure interactions. *Ph.D. Thesis*, Brown University, in progress.
21. Xiu D, Karniadakis GE. Modeling uncertainty in flow simulations via generalized polynomial chaos. *Journal of Computational Physics* 2003, at press.
22. Karniadakis GE, Sherwin SJ. *Spectral/hp Element Methods for CFD*. Oxford University Press: Oxford, 1999.
23. Karniadakis GE, Israeli M, Orszag SA. High-order splitting methods for incompressible Navier–Stokes equations. *Journal of Computational Physics* 1991; **97**:414.
24. Chorin AJ. Hermite expansion in Monte-Carlo simulations. *Journal of Computational Physics* 1971; **8**:472–482.
25. Orszag SA, Bissonnette LR. Dynamical properties of truncated Wiener–Hermite expansions. *Physics of Fluids* 1967; **10**:2603.
26. Gottlieb D, Orszag SA. *Numerical Analysis of Spectral Methods*: *Theory and Applications*. CBMS-NSF, SIAM: Philadelphia, PA, 1977.
27. Boyd JP. The rate of convergence of Hermite function series. *Mathematics of Computation* 1980; **35**:1039–1316.
28. Tang T. The Hermite spectral methods for Gaussian-type functions. *SIAM Journal of Science and Computation* 1993; **14**:594–606.
29. Xiu D. Generalized (Wiener–Askey) polynomial chaos. *Ph.D. Thesis*, Brown University, in progress.
30. Askey R, Wilson J. Some basic hypergeometric polynomials that generalize Jacobi polynomials. *Memoirs of the American Mathematical Society* 1985; **319**.

